Synthesis and dielectric characterisation of triiodide perovskite methylammonium lead iodide for energy applications

S. K. Mahapatra[1] , N. Saykar[1], I Banerjee[2], P. R. Hobson[3], A. K. Sharma[4] , A. K Ray[3]

[1] Centre for Physical Sciences, Central University of Punjab, Bathinda-151001, Punjab, INDIA

[2] The Department of Physics, Birla Institute of Technology, Mesra, Ranchi-835215, INDIA

[3] Department of Electronic and Computer Engineering, Brunel University London, Uxbridge, Middlesex UB8 3PH, UK

[4] United States Air Force Research Laboratory, Space Vehicles Directorate, SE Kirtland AFB, NM 87117 USA.

Abstract

Impedance spectroscopic measurements on spin coated 550 nm thick perovskite films sandwiched between titanium oxide (TiO_2) deposited on fluorine doped indium tin oxide (FTO) glass substrates and with a platinum (Pt) counter electrode have been performed to determine the influence of the percentage of PbI_2 in methylammonium lead iodide ($CH_3NH_3PbI_3$) compounds. These compounds with perovskite structure have been synthesized by weaving methylammonium iodide (CH_3NH_3I) and lead iodide (PbI_2) in two different weight ratios of 1:4 and 3:7. The surface grains are found from the scanning electron microscoping images to have become relatively larger with increasing PbI_2 content in spincoated perovskite film. Nearly 2% increase in optical band gap has been observed with increasing weight ratio of PbI_2 content from1:4 to 3:7 .

Key Words: Gibbs free energy, Kubelka-Munk function, charge transfer resistance, hopping transport, dielectric loss

Corresponding author: S. K. Mahapatra: skmahapatra741973@gmail.com

1.   Introduction

The development of hybrid organic/inorganic perovskite solar cells have seen rapid growth in recent years due to their dramatic increase in power conversion efficiency (PCE) ~ 20% in very short interval of time [1]. The typical configuration of these cells consists of multilayered structures on a transparent substrate carrying electron-selective layer (titanium dioxide (TiO_2)), perovskite absorber (triiodide perovskite methylammonium lead iodide ($CH_3NH_3PbI_3$)), hole transport layer and noble metal counter electrode. The charge mobility is found to increase from 3.2×10^{-4} $cm^2 V^{-1}s^{-1}$ to 7.1×10^{-4} $cm^2V^{-1}s^{-1}$ from both linearly increasing voltage and time of flight measurements,for 250 nm ambipolar triiodide perovskite such as methylammonium lead iodide ($CH_3NH_3PbI_3$) single layer films when it forms a 400 nm thick bilayer with phenyl-C61-butyric acid methyl ester film due to intercalation and aggregation between the layers [2]. The high performance of $CH_3NH_3PbI_3$ solar cells may be attributed to the suppressed recombination, long life of mobile charges and the absence of shallow traps. Other cell structures using the perovskite materials methylammonium lead iodide ($CH_3NH_3PbI_3$) and $CH_3NH_3PbI_3xClx$) are exploited and developed due to their excellent photovoltaic properties including long balanced carrier diffusion lengths (100 –1000 nm) [3], band gap compatibility with the solar spectrum, ambipolar charge transport, [4] low leakage current, strong solar absorption [5] and high capacitance with compatible conductance; and have gained importance in solar cells. The comparison of photoactive material is also an important factor for charging and discharging capability. A certified efficiency of 12.8% was achieved by perovskite solar cells using a carbon electrode, leading to low cost, stability and abundance [6]. From this perspective, properties such as UV absorption, capacitance, conductance and dielectric loss of the perovskite material have a significant role in development of organic/inorganic solar cells. In addition to this, the most significant methods like Transient

Photovoltage (TPV), differential capacitance, charge extraction, current interrupt, and chronophotoamperometry are used to study the optoelectronic properties of solar cells [7].

We report here the synthesis of energy harvesting perovskite materials using two different weight ratios of methylammonium iodide (CH_3NH_3I) and lead iodide (PbI_2) and their morphology and optical properties in thin film forms. As shown in Figure 1(a), the sandwich configurational device structures are fabricated by spin coating perovskite on TiO_2 coated fluorine doped ITO substrates with a sputtered platinum (Pt) film as the counter electrode. Dielectric relaxation spectroscopy involving the measurement of AC electrical response over a wide frequency range provides information on the conductivity of thin films in terms of structural homogeneity and stability considering the relative contribution of grain, grain boundary and defect states [8].

2.   Experimental Details

Following the well- established synthetic route [9, 10], methylammonium iodide CH_3NH_3I was synthesized through the stirring-assisted chemical reaction of commercially available reagents methylamine (Sigma Aldrich Product Number: 534102,) and hydroiodic acid (Product Number: 210021) at a molar ratio of 1.2: 1 in an ice bath for 2 hours. The final product was then dried in vacuum. A PbI_2 precursor solution was synthesized by dissolving 1g of PbI_2 in 2.75g of dimethyl formamide (DMF). The product obtained was washed three times with diethyl ether and recrystallized using a mixture of methanol and diethyl ether. Perovskite absorbers were obtained by mixing CH_3NH_3I with PbI_2 precursor in weight% ratio of 1:4 (Perovskite I) and in wt.% of 3:7 (Perovskite II) respectively then subjected to 12 hours of stirring with γ-butyrolactone (Sigma Aldrich Product Number: B103608) at 60 °C for 12 hours. The white, crystalline product formed at room temperature was then filtered and dried in a vacuum oven for 12 hours. A high resistance, hole-locking, buffer layer of TiO_2 on FTO was prepared using 0.15 M and 0.3 M solution of

3

titanium diisopropoxide bis(acetylacetonate) (75% in 2-propanol, Sigma Aldrich) by spin coating, then heating at 500 ^{o}C for 30 minutes. After cooling to room temperature, the FTO substrate was dipped in a 0.04 M aqueous solution of titanium tetrachloride (TiCl$_4$) at 70°C for 30 minutes, rinsed with water and dried at 500 ^{o}C for 20 minutes. The resulting 550 nm thick perovskite layers were then deposited onto the TiO$_2$ layer by the spin coating method. The counter electrode platinum (Pt) films of thickness ~50 nm was deposited on the top of perovskite layers by RF sputtering at 5×10^{-3} torr to complete the structure of Figure 1(a) . The effective cross-sectional area of the device is 0.09 cm^2.

The surface microstructure and chemical composition of the samples were investigated using a Scanning Electron Microscope (SEM) (Model: JSM 6390LV) fitted with an X-Max^N detector for energy dispersive X-ray spectroscopic (EDS) analysis. The diffuse reflectance spectra of perovskite layers were recorded using UV-Vis spectrometer (Perkin Elmer model 20) in the wavelength (λ) range between 400 nm and 1000 nm at 15 nm per minute. The complex impedance of the FTO/TiO$_2$/CH$_3$NH$_3$PbI$_3$/Pt device was measured under dark conditions using an impedance analyser (Solartron model 1260) in the frequency range of 10 Hz to 1 MHz with signal amplitude 0.1 V$_{rms}$.

3.   Results

SEM images show the presence of the network morphology of small clusters in Perovskite I (Figure 2 (a)) with a random distribution of pores, exhibiting large number of discontinuous grain boundaries. The Perovskite II film surfaces, on the other hand, consist of large, densely packed clusters (Figure 2 (b)). The presence of C, Pd and I can be seen in EDS spectra in Figure 2 (c) and (d) for Perovskite I and Perovskite II, respectively. Similar observations are reported for

CH$_3$NH$_3$PbI$_{3-x}$Cl$_x$ with different % of chloride, showing the improved film coverage of the perovskite layer prepared with low concentration of chloride [11].

Diffuse reflectance spectra within the UV and visible region in Figure 3(a) shows a nearly steady intensity of reflectance (R) from both types of perovskites for the wavelength range of 400 nm < λ < 760 nm followed by sharp rise between 760 nm and 860 nm. The reflectance becomes constant again for wavelengths longer than 860 nm. Similar behaviour has recently been reported for solution processed CH$_3$NH$_3$PbI$_3$, showing a steep rise in diffuse reflectance near $\lambda \approx 760 nm$ [12]. The reflectance increases with increasing percentage of PbI$_2$ content. However this effect becomes visibly pronounced in the low photon energy ($h\nu$) regime for wavelength λ < 760 nm in comparison to the high energy regime corresponding to the wavelength $\lambda \leq 760\ nm$. The absorption in Perovskite II is higher than Perovskite I over the entire energy. The porosity control is found to be important for controlling the UV absorption characteristics [13]. As observed in the SEM studies, the porosity in the morphological structure of Perovskite II is small. This offers larger optical absorption surface area.

The frequency dispersions of conductance, capacitance and dielectric loss of Perovskite I and Perovskite II were obtained from the impedance spectroscopic measurements on the FTO/TiO$_2$/Perovskite/Pt structure. The behavior of the Z modulus for Perovskite I and Perovskite II is shown in Figure 4. The plots of conductivity σ_{ac} vs frequency f on semilogarthimic-linear scales in Figure 5 shows a monotonically non-linear increase of σ_{ac} with frequency f for the range 10 Hz $\geq f \leq$ 100 kHz for both samples. Thereafter σ_{ac} approaches frequency independent values for $f \geq$ 100 kHz. This is attributed to the hopping of charge carriers between randomly distributed localized states through the perovskites [14].

Discussions

The relative atomic percentage of iodide to lead is found to be lower in Perovskite I than that of Perovskite II. With the increase of % of PbI_2, the relative decrease in % of CH_3NH_3I is believed to be responsible for enhancement of Gibbs free energy to form nucleation of perovskite [15]. As a result, the grain sizes became larger in Perovskite II. The relative atomic percentage of iodide to lead is found to be lower in Perovskite I than that of Perovskite II (Figure 2 (c) and (d)). Figure 3(b) shows the Tauc plots in the terms of the transformed Kubelka-Munk function $hvF(R)$

$$[F(R)hv]^p \propto (hv - E_g) \tag{1}$$

where $F(R) = \frac{(1-R)^2}{2R}$ is proportional to the extinction coefficient [16]. The index $p = 2$ implies the occurrence of optical absorption in the perovskite via direct band transition. v and h are the optical frequency and Plank constant. Values of 1.49 eV and 1.46 eV are determined for the optical bandgap E_g for Perovskite I and Perovskite II, respectively from the intercept on the abscissa at the zero ordinate. Similar changes in optical band gap have been observed for perovskite films, prepared by dipping PbI_2 films into different concentrations into methylammonium lead iodide at a fixed time interval of 20 min.[17].

The equivalent electric circuit of FTO/TiO$_2$/ perovskite/Pt is shown in Figure 1(b), consisting of combination of one parallel R_pC_p network in series with the sheet resistance R_s. The overall charge transfer resistance R_p of the cell includes the contribution on the $TiO_2/CH_3NH_3PbI_3/Pt$ interfaces and $CH_3NH_3PbI_3$ layer. C_P indicates the corresponding charge storage capacitance. R_S, C_P and R_P of the electrical equivalent circuit were estimated using Zview software [18] and their values for both perovskites are shown in Table 1. Both values of C_P and R_P are higher for Perovskite I than Perovskite II, implying the charge flow is relatively easier with the increasing content of PbI_2.

The frequency dependence of the equivalent impedance is given by [19]

$$Z_{eq}(w) = R_S + \frac{R_P}{1 + jwR_PC_P}$$

(2)

where ω is the angular frequency of AC signal. R_S is series resistance, R_P Parallel resistance and C_P parallel capacitance. The real part and imaginary part of the complex impedance determined from the above equation are given by

$$\text{Re}(w) = R_S + \frac{R_P}{1 + wR_P^2C_P^2}$$

(3)

$$\text{Im}(w) = \frac{wR_P^2C_P}{1 + w^2R_P^2C_P^2}$$

(4)

The σ_{ac} of Perovskite II is observed to be larger by approximately one order of magnitude than that of Perovskite I in the frequency region of $10\,\text{Hz} \geq f \leq 10\,\text{kHz}$. The conductance of Perovskite I with random porous morphologies is smaller than that of Perovskite II. This significant difference in σ_{ac} between two types of the perovskite film is consistent with their SEM images and EDS analysis indicating the relative porosity and % PbI_2 in Perovskite I and II films [20].

The frequency dispersion of capacitance C_{ac} in Figure 6 for both the perovskites have been attributed due to charge storage capacity in the structure. A sharp fall of capacitance C_{ac} with frequency f can be seen from Figure 6 in a frequency range of 10 Hz to 1 kHz and the value of C_{ac} is one order magnitude higher for Perovskite I than Perovskite II. Both spectra converge at high frequency f > 1kHz to a very low value in order of 1 nF. This is believed to be the geometrical capacitance of the device containing perovskite absorbing layer [21]. This produces a value of nearly 7 for the relative dielectric constant . The dielectric loss of Perovskite I and Perovskite II is shown in Figure 7. The dielectric loss of Perovskite II is higher than that of Perovskite I which signifies that the leakage current in Perovskite II is higher than Perovskite I.

7

Ion polaristion and ion migration may contribute to the low frequency tanδ whereas the ion vibration which causes the high frequency dielectric loss is found to decrease at higher values of frequency $f \geq 10$ kHz. The increase in lead concentration reduces the dielectric loss, possibly due to dipolar polarization, trap states and electrode polarization [22].

5   Conclusion

Environmentally friendly, low-cost, one step deposition method has been successfully employed for fabrication of hybrid inorganic-organic perovskite materials suitable for harvesting solar energy. It is shown that the morphological, optical and electrical properties may be tuned by changing the % of PbI_2 content in perovskite films. The frequency dispersion behaviors of conductivity and capacitance are complimentary to each other. The materials having high absorption coefficient, band gap compatibility with the solar spectrum, low leakage current, high capacitance with compatible conductance are very important for solar cell with increased efficiency. The tuning of capacitance with the % of $PbI2$ is expected to contribute to storage capacity in the development of the charge different storage capacity.

References:

[1]   J. P. Correa-Baena, M. Saliba, T. Buonassisi, M. Graetzel, A. Abate, W. Tress, A. Hagfeldt, Promises and challenges of perovskite solar cells. *Science* **358 (6364)**, , 739-744 (2017).

[2]   Y. Chen, J. Peng, D. Su, X. Chen, and Z. Liang, Efficient and Balanced Charge Transport Revealed in Planar Perovskite Solar Cells. *ACS Appl. Mater. Interfaces* **7(8)**, 4471-4475 (2015).

[3]   S. D. Stranks, G. E. Eperon, G. Grancini, C. Menelaou, M. J. P. Alcocer, T. Leijtens, L. M. Herz, A. Petrozza, H. J. Snaith, Electron-Hole Diffusion Lengths Exceeding 1 Micrometer in an Organometal Trihalide Perovskite Absorber. *Science* **342(6156),** 341-344 (2013).

[4]   G. C. Xing, N. Mathews, S. Y. Sun, S. S. Lim, Y. M. Lam, M. Graetzel, S. Mhaisalkar, T. C. Sum, Long-Range Balanced Electron and Hole-Transport Lengths in Organic-Inorganic $CH_3NH_3PbI_3$. *Science* **342 (6156),** 344-347 (2013).

[5]   M. A. Green, A. Ho-Baillie, H. J Snaith, The Emergence Of Perovskite Solar Cells. Nat. Photonics *Nat. Photonics* **8 (7),** 506-514 (2014).

[6]   J. H. Im, C. R. Lee, J. W. Lee, S. W. Park, N. G. Park, 6.5% Efficient Perovskite Quantum-Dot-Sensitized Solar Cell. *Nanoscale* **3 (10)**, 4088 -4093 (2011).

[7]   Z. Li, S. A. Kulkarni, P. P. Boix, E. Z. Shi, A. Y. Cao, K. W. Fu, S. K. Batabyal, J. Zhang, Q. H. Xiong, L. H. Wong, N. Mathews, S. G. Mhaisalkar, Laminated Carbon Nanotube Networks for Metal Electrode-Free Efficient Perovskite Solar Cells. *ACS nano* **8 (7)**, 6797-6804 (2014);

[8]   C. F. Han, K. Wang, X. X. Zhu, H. M. Yu, X. J. Sun, Q.Yang, B. Hu, Unraveling Surface And Bulk Trap States In Lead Halide Perovskite Solar Cells Using Impedance Spectroscopy. *J. Phys. D-Appl. Phys.* **51(9)**, 095501 (2018)

[9]   Y. X. Zhao, A. M. Nardes, K. Zhu, Mesoporous Perovskite Solar Cells: Material Composition, Charge-Carrier Dynamics, And Device Characteristics. *Faraday Discuss.* **176**, 301-312 (2014)

[10]   W. Y. Xie, Y. M. Wang, X. P. Zhang, Synthesizing Conditions For Organic-Inorganic Hybrid Perovskite Using Methylammonium Lead Iodide. *J. Phys. Chem. Solids* **105,** 16-22 (2017)

[11]   Y. C. Huang, C. S. Tsao, Y. J. Cho, K. C. Chen, K. M. Chiang, S. Y. Hsiao, C. W. Chen, C. J. Su, U. S. Jeng, H. W. Lin, Insight into Evolution, Processing And Performance Of Multi-Length-Scale Structures In Planar Heterojunction Perovskite Solar Cells. *Sci. Rep.* **5,** 13657, (2015).

[12] H. S. Kim, C. R. Lee, J. H. Im, K. B. Lee, T. Moehl, A. Marchioro, S. J. Moon, R. Humphry-Baker, J.-H.Yum, J. E Moser, M. Graetzel, N. G. Park, Lead Iodide Perovskite Sensitized All-Solid-State Submicron Thin Film Mesoscopic Solar Cell With Efficiency Exceeding 9%. *Sci Rep* **2**, 591 (2012)

[13] S. F. Zhuo, J. F. Zhang, Y. M. Shi, Y. Huang and B. Zhang, Self-Template-Directed Synthesis of Porous Perovskite Nanowires at Room Temperature for High-Performance Visible-Light Photodetectors. *Angew. Chem.-Int. Edit.* 54(19) 5693-5696 (2015). **DOI:** 10.1002/anie.201411956

[14] T.C. Sum and N. Mathews, Advancements In Perovskite Solar Cells: Photophysics Behind The Photovoltaics *Energy Environ. Sci.* **7(8)**, 2518 -2534 (2014).

[15] M. Alidaei, M. Izadifard, M. E. Ghazi, V. Ahmadi, Efficiency Enhancement Of Perovskite Solar Cells Using Structural And Morphological Improvement Of CH3NH3PbI3 Absorber Layers. *Mater. Res. Express*, **5(1),** 016412, (2018).

[16] E. L. Simmons Relation of Diffuse Reflectance Remission Function To Fundamental Optical Parameters.*Optica Acta* **19(10)**, 845-851 (1972).

[17] S. A. Kulkarni, T. Baikie, P. P. Boix, N. Yantara, N. Mathews, S. Mhaisalkar, Band-Gap Tuning Of Lead Halide Perovskites Using A Sequential Deposition Process. *J. Mater. Chem. A* **2(24)**, 9221-9225 (2014)

[18] H. Y. Wei, J. Y. Xiao, Y. Y. Yang, S. T. Lv, J. J. Shi, X. Xu, J. Dong, Y. H. Luo, D. M. Li, Q. B. Meng, Free-Standing Flexible Carbon Electrode for Highly Efficient Hole-Conductor-Free Perovskite Solar Cells *Carbon* **93**, 861-868 (2015)

[19] S. S. Mali, C. S. Shim, H. Kim, P. S. Patil, C. K. Hong, In Situ Processed Gold Nanoparticle-Embedded TiO_2 Nanofibers Enabling Plasmonic Perovskite Solar Cells To Exceed 14% Conversion Efficiency. *Nanoscale,* **8(5)**, 2664-2677 (2016).

[20] J. Liu, C. Gao, X. L. He, Q. Y. Ye, L. Q. Ouyang, D. M. Zhuang, C. Liao, J . Mei, W. M. Lau, Improved Crystallization of Perovskite Films by Optimized Solvent Annealing for High Efficiency Solar Cell.. *ACS Appl. Mater. Interfaces,* **7(43)**, 24008-24015 (2015)' H.

[21] H. S. Duan, H. P. Zhou, Q. Chen, P. Y. Sun, S. Luo, T. B. Song, B. Bob, Y. Yang, The identification and characterization of defect states in hybrid organic-inorganic perovskite photovoltaics. *Phys. Chem. Chem. Phys.* **17 (1),** 112-116 (2015).

[22]   O. Almora, I. Zarazua, E. Mas-Marza, I. Mora-Sero, J. Bisquert, Garcia-Belmonte, G.
        Garcia-Belmonte. Capacitive Dark Currents, Hysteresis, and Electrode Polarization in
        Lead Halide Perovskite Solar Cells. *J. Phys. Chem. Lett.* **6 (9)**, 1645-1652 (2015).

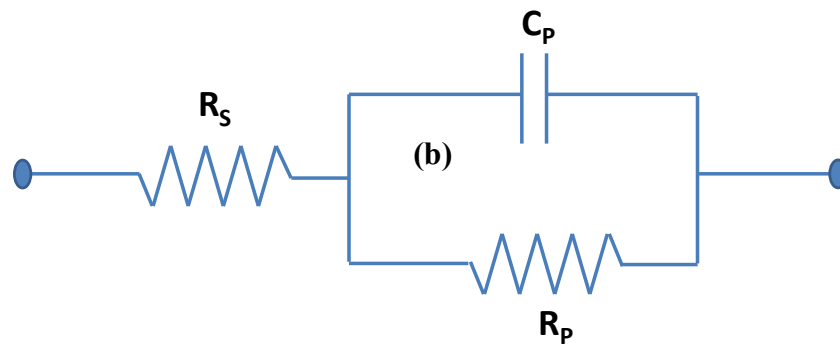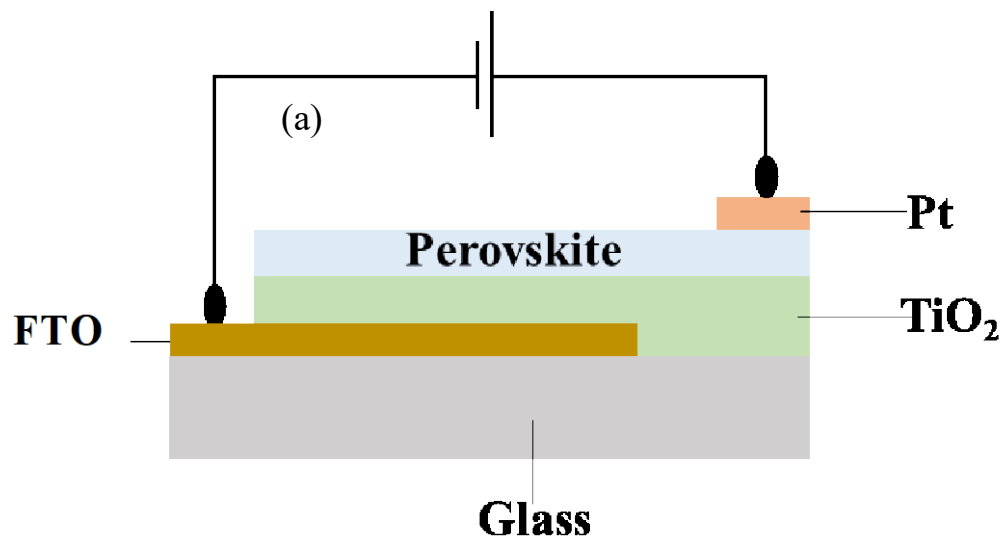**Figure Captions**

Figure 1.   (a) Schematic FTO/TiO$_2$/ Perovskite/Pt structure for electrical measurement and (b)
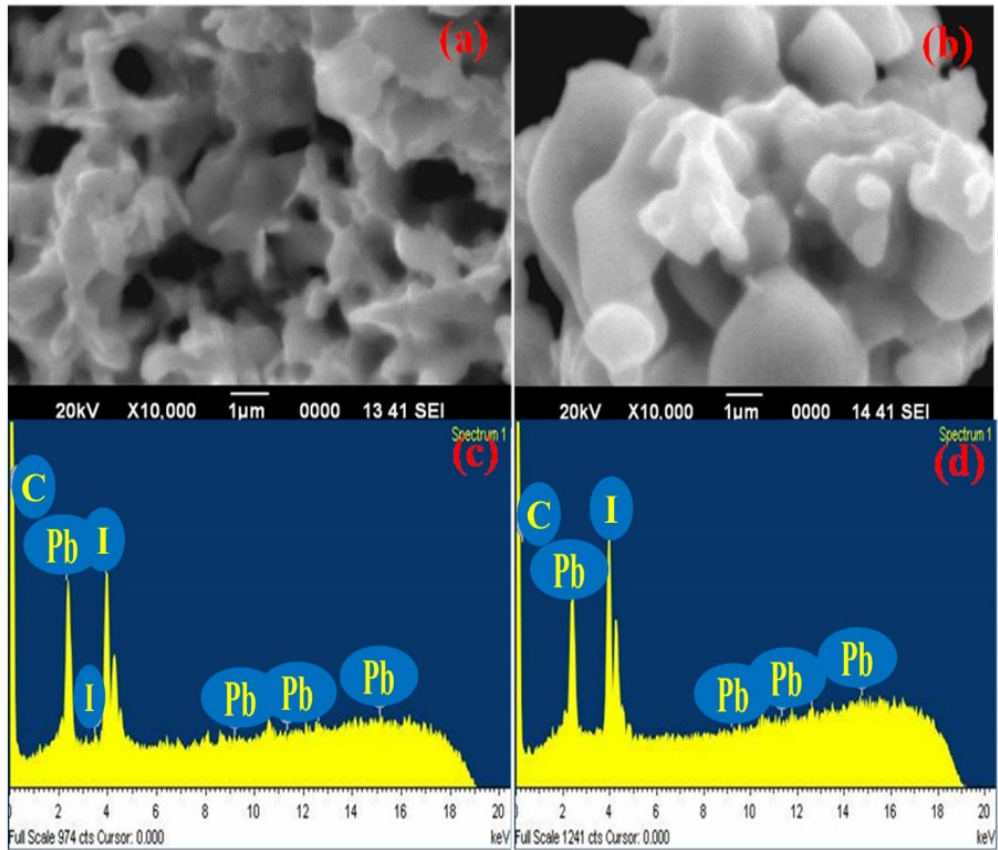   electrical equivalent circuit of the structure

Figure 2.   SEM and EADX of Perovskite I (a) and (c), Perovskite II (b) and (d) respectively
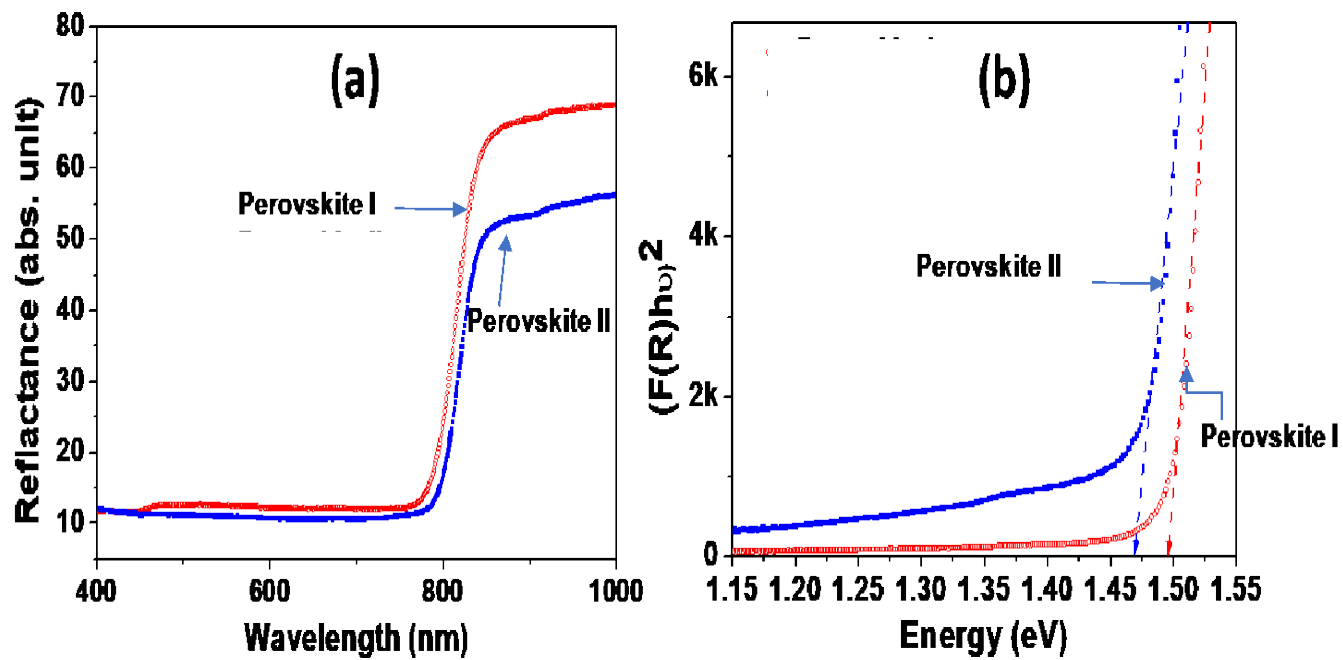
Figure 3.   (a) Diffuse reflectance spectra with UV visible of Perovskite I and Perovskite II and
               (b) Tauc plots of Perovskite I and II material.

Figure 4.   Modulus of impedance vs frequency plots with fitted curves of Perovskite I
               (broken line with open circle) and Perovskite II (solid line with solid rectangle)

Figure 5.   Conductivity vs frequency plots with fitted curve of Perovskite I and Perovskite II

Figure 6.　Capacitance vs frequency plots of Perovskite I (open circle) and Perovskite II (solid rectangle)

Figure 7.　The dielectric loss $\tan\delta$ of Perovskite I and Perovskite II

Table 1: Fitted Value of R_s, C_p and R_p for Perovskite I and Perovskite II

Perovskite	R_s	C_p	R_p
Perovskite I	0.25 MΩ	4.5 nF	50 MΩ
Perovskite II	0.3 MΩ	0.11 nF	20 MΩ

Figure 1.   (a) Schematic FTO/TiO$_2$/ Perovskite/Pt structure for electrical measurement and (b) electrical equivalent circuit of the structure

Figure 2. SEM and EADX of Perovskite I (a) and (c), Perovskite II (b) and (d) respectively

Figure 3.: (a) UV visible reflectance spectra of Perovskite I and Perovskite II and (b)) Tauc plots of Perovskite I and II material.
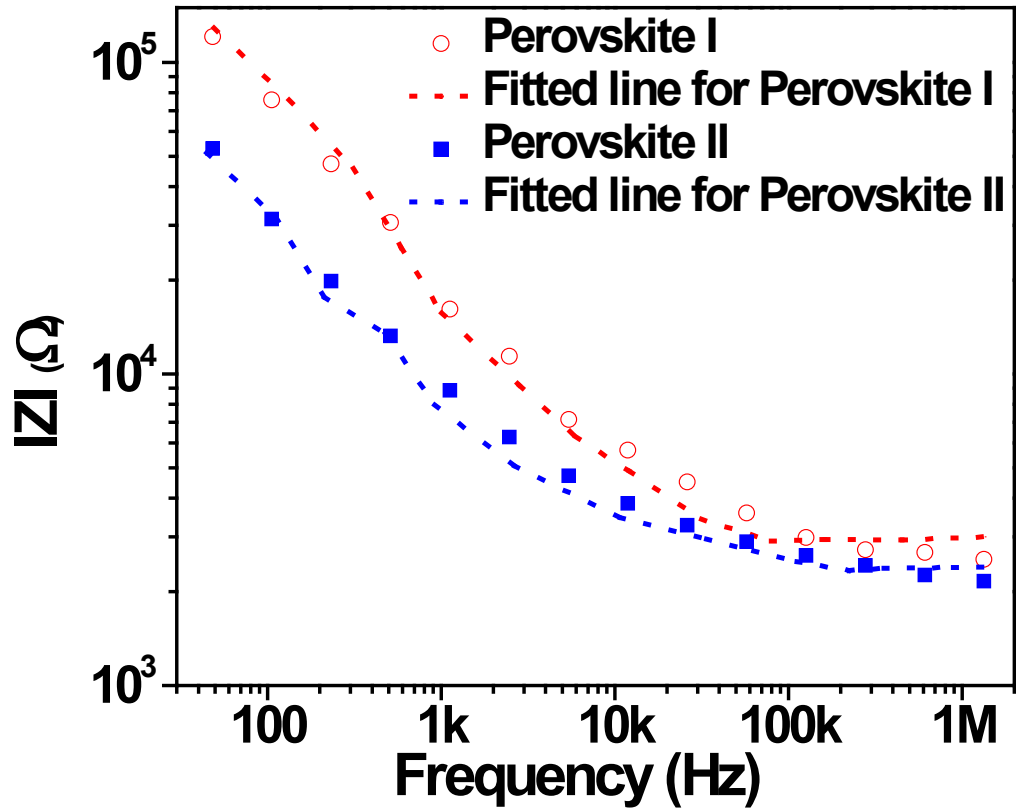
Figure 4.   Modulus of impedance vs frequency plots with fitted curves of Perovskite I (open circle) and Perovskite II (solid rectangle)
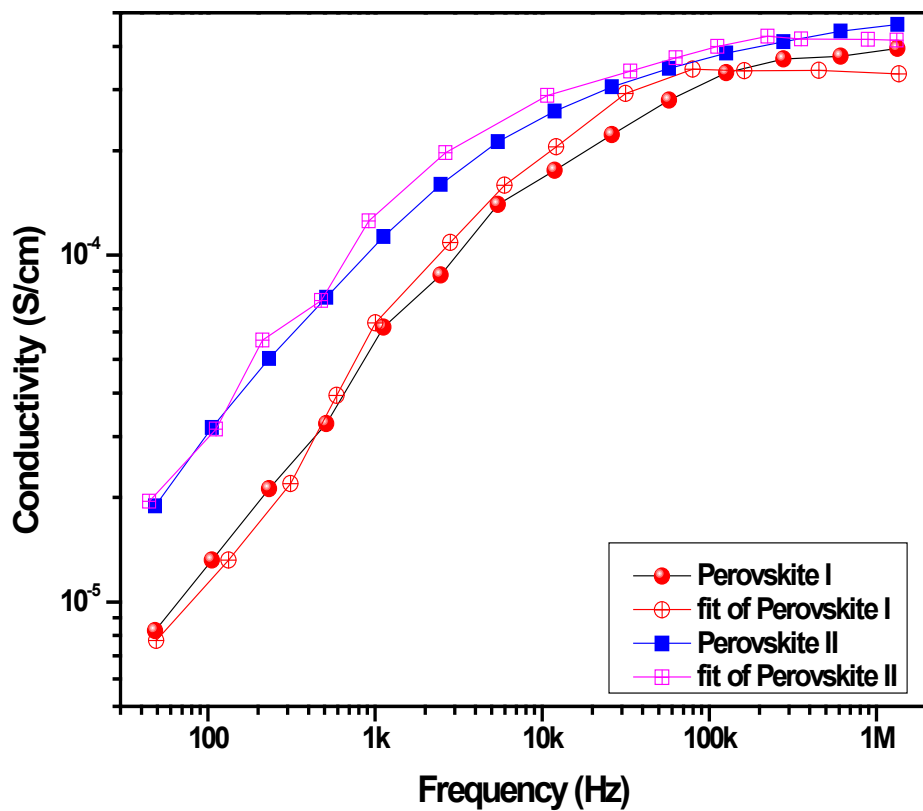
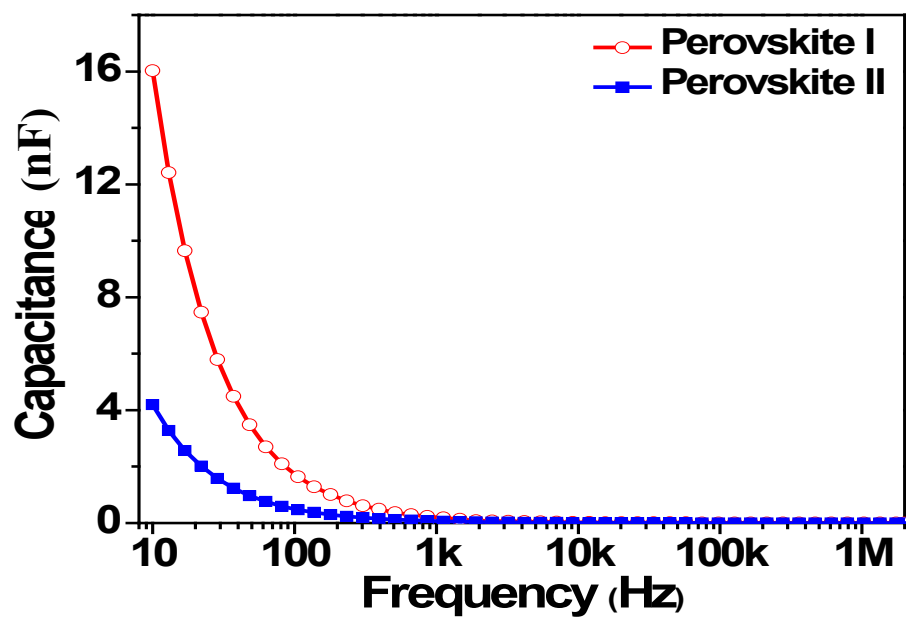Figure 5.   Conductivity vs frequency plots with fitted curve of Perovskite I and Perovskite II

Figure 6.   Capacitance vs frequency plots of Perovskite I (open circle) and Perovskite II (solid rectangle)
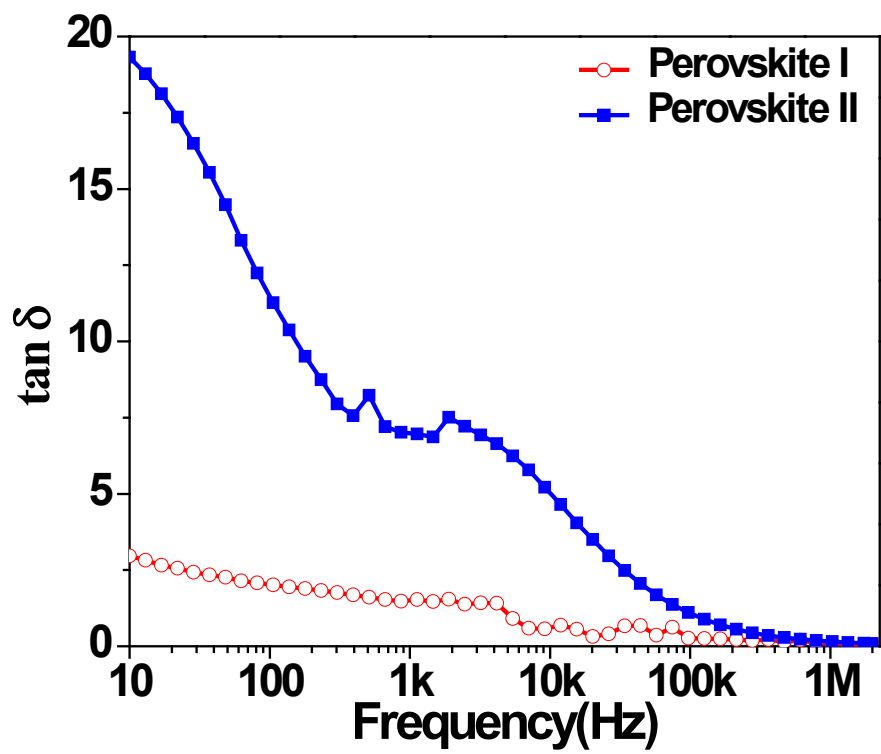
Figure 7. Dielectric loss spectra of Perovskite I (open circle) and Perovskite II (rectangle)